Received: 29 July 2022 | Revised: 26 July 2023 | Accepted: 22 August 2023

DOI: 10.1002/pip.3739

SPECIAL ISSUE ARTICLE

PROGRESS IN PHOTOVOLTAICS WILEY

Towards a graphene transparent conducting electrode for perovskite/silicon tandem solar cells

John O'Sullivan | Matthew Wright | Xinya Niu | Poppy Miller | Peter R. Wilshaw | Ruy S. Bonilla

Department of Materials, University of Oxford, Oxford, UK

Correspondence
Ruy S. Bonilla, Department of Materials, University of Oxford, Oxford, OX1 3PH, UK.
Email: sebastian.bonilla@materials.ox.ac.uk

Funding information
Engineering and Physical Sciences Research Council, Grant/Award Number: EP/V038605/1; Royal Academy of Engineering; John Fell Fund, University of Oxford

Abstract

Indium-based transparent conducting electrodes (TCEs) are a major limiting factor in perovskite/silicon tandem cell scalability, while also limiting maximum cell efficiencies. In this work, we propose a novel TCE based on electrostatically doped graphene monolayers to circumvent these challenges. The electrode is enabled by a thin film dielectric that is charged and interfaced to a graphene film, optimally exploiting electrostatic doping. The field effect mechanism allows the modulation of charge carriers in monolayer graphene as a function of charge concentration in the dielectric thin film. Electrostatic charge was deposited on SiO_2 membranes, and graphene transferred onto them exhibited a reduction in sheet resistance because of the induced charge carriers. We show a reduction in sheet resistance of graphene by 60% in just 3 min of dielectric charging, without impacting the transmission of light through the film stack. Hall effect measurements indicated that the mobility of the films was not significantly degraded. The deposition of negative electrostatic charge reversed this effect, allowing for precise tunability of charge concentration from n- to p-type. We develop a model to determine the required sheet resistance of a graphene TCE with 97% transmittance in a perovskite/silicon tandem cell. As the technique here reported does not impact transmittance, a graphene TCE with a sheet resistance below 50 Ω/□ could enable efficiencies up to 44%, presenting a promising alternative to indium-based TCEs.

KEYWORDS
electrostatic doping, graphene, ITO, IZO, tandem solar cells, transparent conducting oxides

1 | INTRODUCTION

1.1 | Transparent conducting electrodes (TCEs) in perovskite/silicon tandem cells

The efficiency of single-junction silicon solar cells is approaching the practically achievable limit of 29.4%.[1] Yoshikawa et al achieved an efficiency of 26.7% with an IBC silicon heterojunction (SHJ) design,[2] and LONGi Solar have demonstrated efficiencies up to 26.81% for large-area industrially processed SHJ cells.[3] As these efficiencies approach the practical limit, a tandem solar cell design can be employed to circumvent the limitations of single-junction cells.[4,5] In a tandem cell, two cells of differing band gap (E_g) are stacked together to more effectively harvest solar energy. This increases the maximum theoretical efficiency potential for a tandem cell with a silicon bottom cell to 45.1% if connected in the two-terminal configuration or 45.3%

if connected in the four-terminal configuration.[6–8] A promising combination of tandem subcells for widespread terrestrial applications involves using a large E_g perovskite top cell and a lower E_g SHJ bottom cell. Perovskites are particularly promising as the top cell in a tandem because of the large absorption coefficient,[9] large V_{OC} potential,[10] and readily tuneable E_g.[11] Of the available single-junction silicon cell architectures, the SHJ design is particularly advantageous in a tandem architecture. It has the highest efficiency potential, and the a-Si passivating layers are conductive, which avoids the requirements for localised interconnection.[2,12] However, perovskites and the passivating layers in SHJ cells both have poor lateral conductivity; hence, they require additional layers with high lateral conductivity for efficient charge carrier collection at metal fingers.[13] Such layers must also have high transmittance to minimise parasitic absorption losses. This trade-off between light absorption and conductivity has been the subject of decades of research.[14–16] Photocurrent losses in 'transparent conducting electrodes' (TCEs), referred to as parasitic absorption, can represent a major efficiency loss, contributing to a reduction of single-junction module efficiency by $10\%_{rel}$–$25\%_{rel}$.[17] Additionally, the most frequently used TCEs, indium zinc oxide (IZO) and indium tin oxide (ITO), use scarce, unsustainable indium, which severely limits the manufacturing potential of cell designs requiring it.[18,19] Producing low-cost, sustainable TCEs with optimised properties is crucial in achieving high-efficiency tandems with widespread applicability. Such innovations could enable an accelerated uptake of renewable energy and reduce global carbon emissions. Graphene is a material that is increasingly low-cost to produce and has a transmittance that exceeds that of ITO and IZO, yet has limited applications as a transparent conductor because of its relatively high resistivity.[20] In this work, we demonstrate that a sufficiently-doped high-transmittance graphene layer could circumvent the issues with conventional TCEs that are currently limiting perovskite/silicon tandem uptake and efficiency losses.

Compared with single-junction cells, TCEs in tandem cells have more stringent optical requirements.[21] All perovskite/silicon tandem configurations require a front TCE with high transmittance to light from ≈280 to 1100 nm to maximise light absorption across the air-mass 1.5 global (AM1.5G) spectrum in both perovskite and silicon subcells. In a single-TCE two-terminal monolithic perovskite/silicon tandem, its TCE can contribute >1 mA/cm^2 J_{SC} loss because of parasitic absorption, equivalent to $\sim 1\%_{abs}$ loss in efficiency.[22,23] The two- and four-terminal mechanically-stacked and three-terminal monolithic tandem configurations usually require one or two additional TCEs between the subcells, from which parasitic absorption may cause ~3–4 mA/cm^2 loss in J_{SC}.[21,22,24] This places significant pressure on TCE performance. As TCEs tend to be one of the most expensive components in solar cell fabrication, as well as multiple-terminals increasing balance-of-system costs, the single-TCE two-terminal monolithic configuration is preferable for large-scale commercial applications.[21] The series connection of monolithic two-terminal cells requires current matching between the cells, constraining the bandgaps that can be used. However, the tunability of perovskite band gaps can mitigate this issue.[11] To incorporate bifaciality in tandems, an extra TCE with high infrared (IR) transmittance and efficient light coupling is also needed at the rear.[12] This is essential for high-efficiency SHJ bottom cells. Solar cell manufacturers must balance a trade-off between the high efficiencies of SHJ cells versus the high cost of an additional TCE. Low-cost TCEs with broadband transmittance would serve to eliminate this trade-off and enable higher efficiencies in tandem cell architectures.

Along with requiring broadband transmittance, TCEs in a tandem cell must contribute minimally to the series resistance (R_S) of the cell. TCEs must have a low sheet resistance (R_{sheet}), as well as a low contact resistance to the metal fingers. The R_{sheet} in units of Ω/□ can be approximated, assuming uniform carrier generation, as described by Equation 1:

$$R_{sheet} = \frac{1}{\sigma t} = \frac{1}{\mu n q t}, \quad (1)$$

where σ is electrical conductivity, μ and n are majority carrier mobility and concentration respectively, q is the charge of the majority carrier, and t is the thickness of the film.[15,25] Equation 1 illustrates that to minimise R_{sheet}, one must choose a film with large μ, n and t. However, increasing t reduces transmittance. Similarly, increasing n increases free-carrier absorption (FCA), reducing overall transmittance.[13,26] This motivates the need for TCEs with high mobility, so that R_{sheet} is low without inducing free carrier absorption from high carrier concentrations. These fundamental trade-offs in TCE properties must be balanced for optimum performance in tandem cells.

TCEs in tandems must also be stable and compatible with the processing of other cell materials. Perovskite layers have poor stability to moisture, UV light and temperatures as low as 85°C,[27] whereas SHJ processing must occur at temperatures <250°C because of the poor thermal stability of the amorphous silicon based passivation.[28] TCE materials for tandems must fit within the processing constraints of the other layers. Furthermore, all materials and processing steps in producing a tandem cell must be sustainable, to realise terawatt-scale photovoltaic global production capacity. This would enable notable reductions in global carbon emissions while meeting energy demand.[18]

ITO is the dominant TCE used in optoelectronics.[29,30] This transparent conducting oxide (TCO) has high transmittance to visible light ≈80%–90% because of its low absorption coefficient and low $R_{sheet} \approx 10$–100 Ω/□ because of its high carrier concentration $n \approx 10^{20}$–10^{21} cm^{-3} and moderately high mobility $\mu \approx 20$–50 cm^2/Vs.[31–36] However, this high carrier concentration causes high parasitic FCA in the near-UV and IR regions, which is severely detrimental to tandem performance.[13,26,37] It is therefore critical to prioritise TCOs with high carrier mobility over high carrier concentration to maintain high transmittance with low R_{sheet}.[38] IZO is the most frequently used top TCE in perovskite/silicon tandem because of its high mobility ≈60 cm^2/Vs, but it suffers from reduced transmittance in the ultraviolet–visible (UV–Vis) range.[13] Zirconium oxide doped In_2O_3 (IZRO) is a promising TCO for tandems, with high mobility ≈77 cm^2/Vs.[26,39] It exhibits reduced FCA in the NIR region, resulting in an efficiency increase of $2.3\%_{abs}$ in perovskite/silicon tandems.[26] Similarly, hydrogen-doped indium oxide (IO:H) offers very low FCA because of high mobility ≈100 cm^2/Vs, but suffers from poor stability.[13] Other indium-based TCOs with high mobility and NIR transmittance that

may be suitable for tandems include cerium/hydrogen and tungsten/hydrogen co-doped In_2O_3, although these require high-temperature annealing steps incompatible with many tandem designs.[13,26,40] However, crucially, there are insufficient global indium reserves to meet the demand for future terawatt-scale photovoltaic capacity.[18] Zhang et al calculated that the annual manufacturing capacity for SHJ cells using ITO was only 37 GW.[18] Using perovskite/silicon tandems offers some scope for improvement, yet are limited to just 29–177 GW/year, indicating that indium cannot be used in any significant PV manufacturing capacity.[18,19] This scarcity causes high, fluctuating costs, limiting uptake. Additionally, the demand for ITO-based TCEs is increasing in the consumer electronics industry, for example, in touch screens and LEDs. A high mobility indium-free TCE is hence a critical requirement to facilitate the future deployment of tandem PV cells as part of efforts to reduce global carbon emissions and mitigate anthropogenic climate change.

Indium-free TCOs such as fluorine-doped tin oxide (FTO) and aluminium-doped ZnO (AZO) suffer from high FCA because of low mobility, with AZO additionally suffering from instability.[13,34] Moreover, the relatively expensive sputter deposition process of TCOs damages perovskite layers.[38,41] This necessitates an additional buffer layer such as MoO_x, increasing processing time and costs, and often reducing stability and transmittance.[38,41] Recent work has demonstrated that ITO can be deposited with no critical damage to the underlying perovskite layer, but tends to produce lower quality TCOs than commercial sputtering processes and requires further optimisation.[42–44] Silver nanowires (AgNWs) can be deposited as a dense conductive mesh for carrier transport to metal fingers, leaving voids for light transmission, attaining properties comparable with ITO.[13,45] However, AgNWs suffer from poor stability, and increasing the use of Ag in solar cells is prohibitively expensive and unsustainable.[18,38] Alternatives such as copper nanowires and carbon nanotubes also exhibit poor stability, as well as high contact resistance and poor substrate adhesion.[13,45] A viable indium-free TCE must overcome these issues to achieve success in tandems.

1.2 | Graphene as a TCE

A promising indium-free TCE for tandem solar cells is graphene.[46] From a processing perspective, there are several advantages to using graphene. Graphene is becoming increasingly affordable to produce using chemical vapour deposition (CVD) in dimensions comparable with industrial solar cell processing. Sheets can be processed and deposited using roll-to-roll techniques compatible with perovskite solution and roll-to-roll processing.[32,47] In perovskite cells, CVD graphene has been shown to be safely transferrable without damaging the fragile absorber or frequently used hole-transport layers (HTLs), such as spiro-OMeTAD, P3HT, PEDOT:PSS and NiO_x, maintaining good, defect-free interfaces.[48–55] Similarly, mono- and multilayer-reduced graphene oxide sheets have been effectively deposited directly on perovskite and yielded functioning perovskite cells without a separate HTL.[56] Additionally, graphene flakes have been effectively interfaced as an additive for TiO_2 in perovskite cell ETLs, in this case not acting as the TCE layer.[57,58] Graphene layers have also been incorporated as a TCE layer in SHJ cells without damaging the underlying layers.[59–61] The strong sp^2 carbon bonds in graphene give it high chemical and mechanical stability.[62] Graphene is impermeable to gas and water, providing additional stability as an encapsulating layer for components susceptible to moisture, such as perovskites.[27,62] Graphene is sustainable, consisting entirely of an atomically-thick carbon layer. CVD graphene can be grown on relatively inexpensive copper sheets, which can be reused, requiring less energy and lower carbon emissions to produce than ITO films.[46]

Table 1 displays a comparison between the material properties of monolayer graphene, ITO and IZO. Note that the values are given as ranges, which depend on fabrication conditions. Table 1 serves to highlight the primary differences between these materials. From an optical standpoint, graphene is clearly advantageous, with typical broadband transmittance >97% for monolayer graphene.[63] This is much higher than ITO or IZO and could lead to substantially reduced parasitic absorption losses in a tandem solar cell. Unlocking the potential of graphene could thus substantially improve the efficiency of perovskite/silicon tandems. ITO and IZO are capable of achieving R_{sheet} as low as 10 and 40 Ω/□, respectively, which is required to reduce electrical losses. In contrast, the R_{sheet} of graphene is too high to act as an effective TCE in tandem solar cells. As discussed above, the R_{sheet} is determined by both the carrier concentration and mobility of majority carriers. The mobility of graphene is very high, in the range from 1000 to 40,000 cm^2/Vs on SiO_2 at room temperature.[71] However, the R_{sheet} is limited by its carrier concentration, which is the order of magnitude lower than ITO or IZO. For graphene to

TABLE 1 Comparison of typical material properties of monolayer graphene on SiO_2, ITO and IZO for photovoltaic applications, at standard temperature and pressure.

	Monolayer graphene	ITO	IZO
Transmittance (%)	Up to 97.7, broadband[63–65]	80–90, reduced in IR and UV[31–36]	80–90, reduced in UV–Vis[66]
Sheet resistance (Ω/□)	500–1500[31]	10–100[31–36]	40–100[66]
Thickness (nm)	0.335[67]	100–300[66,68–70]	100[66]
Carrier concentration (cm^{-3})	10^{18}–10^{19}[71]	10^{19}–10^{21}[31–36,70]	1–5 × 10^{20}[13,66]
Sheet carrier concentration (cm^{-2})	10^{11}–10^{12}[71]	10^{14}–10^{16}[31–36]	1–5 × 10^{15}[13,66]
Mobility (cm^2/Vs)	1000–40,000[71]	20–50[31–36]	40–60[13,66]

Abbreviations: ITO, indium tin oxide; IZO, indium zinc oxide; UV–Vis, ultraviolet–visible.

become a viable alternative as a TCE, this critical issue must be resolved.

The conventional approach to increase the carrier concentration in graphene is by chemical doping. However, chemical doping is often unstable, difficult to control and typically reduces the transmittance and mobility of graphene because of the disruption of its lattice by dopant atoms.[25,65,72] Graphene's R_{sheet} can also be reduced if multiple graphene layers are used, but this degrades the transmittance significantly (2.3% transmittance reduction with each layer).[64,65] Lang et al demonstrated that CVD graphene TCE integration in perovskite/silicon tandems is possible without damaging the perovskite layer, but its R_{sheet} was too high.[48] Doping graphene with perovskite HTL materials spiro-OMeTAD, MoO_3, PH3T and PEDOT:PSS in a perovskite cell have been demonstrated, with compatibility possible for perovskite/silicon tandems.[49–52,54] However, these approaches did not lead to a sufficient increase in its carrier concentration, resulting in low efficiencies relative to cells with indium-based TCEs. Doping with $AuCl_3$ in a perovskite cell was shown to reduce the R_{sheet} stack significantly, offering performance that rivals ITO.[55,58] However, aggregated Au particles increase light scattering, minimising the maximum efficiency potential, particularly deleterious if incorporated in a tandem cell stack.[55,58] 'Transfer-free' graphene for flexible substrates was doped using NiO_x, enabling sheet resistances <100 Ω/□, while preserving high transmittance.[53] But this result is limited to flexible substrates and hole carrier transport, limiting its applicability in tandem cells. Therefore, it is critical to develop alternative approaches that can sufficiently dope graphene TCEs in different parts of a tandem device stack, so that carrier concentration is increased and the desired R_{sheet} can be achieved without impacting the transmittance or mobility.

An alternative approach to doping graphene is to use the field effect or electrostatic mechanism. By establishing an electrostatic field in the vicinity of graphene using a gate bias, a mirror charge is induced in it. This increases the carrier concentration and has been shown to reduce R_{sheet} to values as low as 100 Ω/□.[73] In field-effect doping the mobility is reduced, but to a less significant extent than when using chemical doping techniques. In chemical doping, species either directly disturb the graphene lattice structure or cause charge impurity scattering.[31,72,74,75] In field-effect doping, however, the R_{sheet} reduction only occurs when the power supply is switched on, meaning this technique is not applicable in the context of tandem cell fabrication. Paradisi et al demonstrated that under applied bias and high temperature, charged ions could be migrated in a thick glass film to permanently electrostatically dope graphene, enabling carrier concentration modulation $>10^{14}$ cm^{-2}.[76] However, this requires an opaque metal electrode and was only shown to be possible on thick silica films, hindering its applicability for perovskite/silicon tandem cells. In recent years, Bonilla et al demonstrated that using corona charge and solid-state alkali ions, it is possible to permanently embed large concentrations of charge in thin films of SiO_2.[77,78] This establishes a permanent electrostatic field in the thin dielectric film, generating field effect surface passivation that is stable on commercial timescales.[78]

In this work, we reveal how electrostatic corona charge deposited on a thin SiO_2 film can generate a field effect large enough to manipulate the carrier concentration of graphene. Although field-effect doping of graphene has been known for nearly two decades,[73] the key novelty in this work is the way in which the doping is achieved. We introduce here a new technique that we refer to as 'ion-charged dielectric' (ICD) doping. In this case, the magnitude of the electric field effect can be precisely controlled by varying the amount of charge deposited on a dielectric thin film. Figure 1 depicts how this technique can be used to enhance conductivity in graphene, where positive and negative charges induce n- and p-type doping, respectively. This allows for tailored carrier concentration so that low R_{sheet} graphene can be produced without detrimentally affecting transmittance or mobility. The process is rapid, inexpensive and compatible with the processing conditions required of perovskites and SHJ cells. Such developments offer the path towards a viable indium-free, graphene TCE in perovskite/silicon tandem cells.

2 | EXPERIMENTAL METHODOLOGY

Demonstrating ICD-doping of graphene requires the manufacture of a device in which a close interface can be formed between a thin film dielectric and a monolayer of graphene. Figure 2A shows the device architecture used in this work to achieve this. A 0.4 × 0.4 cm^2 CVD monolayer graphene sheet is transferred to a 0.5 × 0.5 cm^2 p-type Si/SiO_2 substrate using a standard wet-transfer method (see Section-S1, Supplementary Material).[79] The 300 nm SiO_2 layer is unsupported

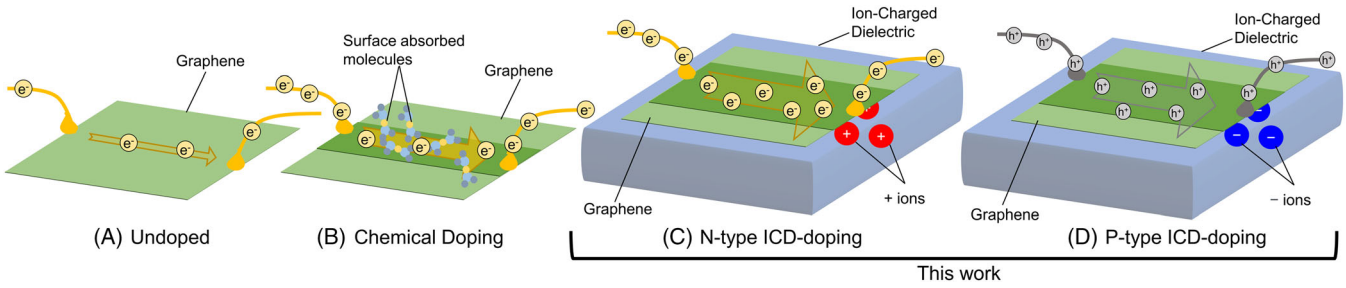

FIGURE 1 Representation of doping in 2D materials using ion-charged dielectrics (ICDs) compared with conventional chemical doping. (A) Undoped. (B) Chemical 'surface absorption' doping. This work: (C) N-type ICD doping and (D) P-type ICD doping. [Colour figure can be viewed at wileyonlinelibrary.com]

in the central 0.5 × 0.5 mm^2 region, referred to as the 'membrane window', which allowed for electrostatic charge deposition. A 1064 nm IR laser (Linxuan LX-A1-20W) was used to remove the graphene from the area around the SiO_2 membrane window. Aluminium metal contacts of thickness 500 nm for electrical characterisation were thermally evaporated at the corners of the graphene using a shadow mask. Samples were stored in a low-pressure chamber purged with nitrogen to minimise moisture-induced degradation and were only removed during characterisation. Figure 2B shows a schematic of the electrostatic doping apparatus, constructed in-house. Devices are placed graphene-side down on a ground electrode, at a known distance over a point discharge electrode. A constant voltage is applied between the ground and discharge electrode. This ionises the air around the discharge electrode and accelerates electrostatic charge towards the sample. Positive applied voltage deposits positively charged corona ions (mostly $(H_2O)_nH^+$) on the surface of the SiO_2 membrane, whereas a negative applied voltage deposits negatively charged corona ions (mostly CO_3^-).[80,81] The quantity of charge deposited is controlled by varying the total time for which the device was held under constant voltage. A KP Technology Scanning Kelvin Probe SKP5050 with a 50 µm tip was used to characterise the quantity of corona charge deposited on the SiO_2 membrane. The sheet resistance of graphene was measured after varying amounts of corona charge were deposited using the Van der Pauw method. The carrier concentration and mobility were calculated by measuring the Hall effect of the films under a perpendicular magnetic field of 0.3 T. For Van der Pauw and Hall effect measurement, signal generation and measurement were carried out using a Keysight B2901A Source measuring unit, controlled via a virtual instrument programmed in LabVIEW. A LabRam Aramis HORIBA Jobin Yvon Raman spectrometer with a 532 nm laser was used to determine the defect density and doping behaviour of the graphene. The transmittance of the graphene film before and after electrostatic doping was determined using an Ocean Optics FLAME-T-XR1-ES spectrophotometer with a DH-2000-BAL light source. All characterisation was carried out in standard laboratory conditions of room temperature and pressure.

This work aims to demonstrate how electrostatic ICD-doping can reduce the sheet resistance of graphene to a level competitive with TCOs without impacting transmittance. As the transmittance of monolayer graphene exceeds ITO and IZO, it is not expected to need as high an R_{sheet} to match the overall performance of ITO films in tandem solar cells, assuming that its high transmittance can be maintained. We present a model depicting tandem cell efficiency as a function of TCE transmittance and R_{sheet} based on the work of Anand et al where an 'exact Figure of Merit' is calculated to compare TCE application in photovoltaic devices.[82] We use this to predict the required sheet resistances for an electrostatically doped monolayer graphene film in a two-terminal monolithic stack tandem cell and compare this with frequently used TCO materials. The details of the model can be found in Sections S6 and S7 of the Supplementary Material.

3 | RESULTS AND DISCUSSION

3.1 | Electrical characterisation

The first step in demonstrating ICD-doping of graphene was to ensure that a concentration of static charge can be built and maintained on top of the free-standing thin film membrane. Figure 3A depicts the contact potential difference (CPD) of the SiO_2 membrane, as it is held under an applied corona voltage of ±30 kV over 16 min of total charging time. As the charging time is increased, the CPD of opposite polarity increases in magnitude. The magnitude of the CPD is proportional to the amount of corona charge deposited on the surface of the SiO_2 membrane.[83] After 6 min at +30 kV, the CPD saturates at about −12 V, whereas after 8 min at −30 kV, the CPD saturates at about +20 V. At this point, no additional charge can be deposited on the film, and the electric field generated is likely to be at its maximum.

Ten hours after positive charging, the CPD measured decayed by just 2.80% (see Figure S1, Section S2, Supplementary Material) Similarly, 12 h after negative charging, the CPD decayed by 7.82% (see Figure S1, Section S2, Supplementary Material). This stability allows

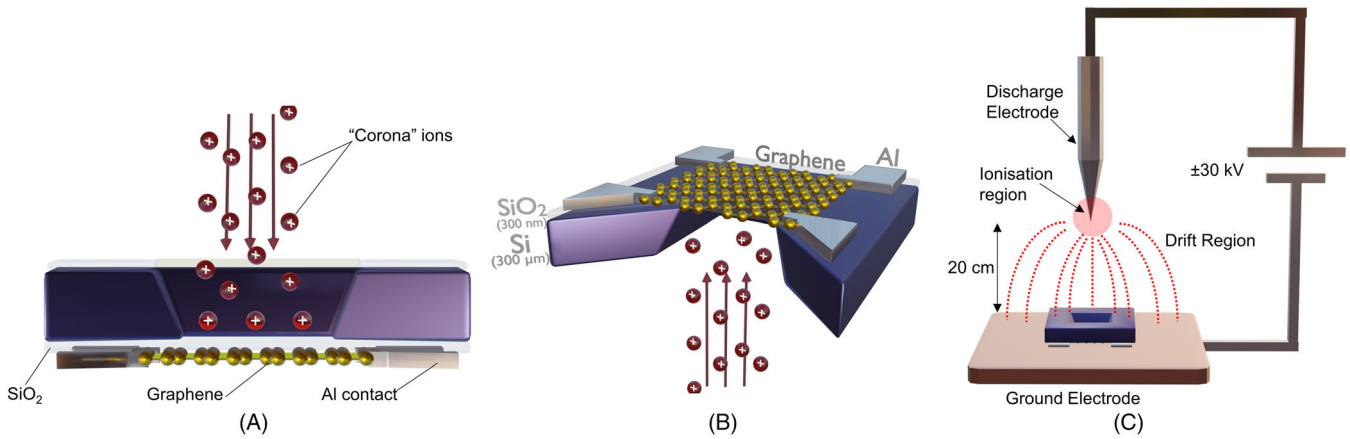

FIGURE 2 Corona charging SiO_2 membrane for graphene doping. (A) Graphene device structure (cross-section). (B) Graphene device structure (3D cutaway view). (C) Apparatus used for corona charging of the SiO_2 membrane. [Colour figure can be viewed at wileyonlinelibrary.com]

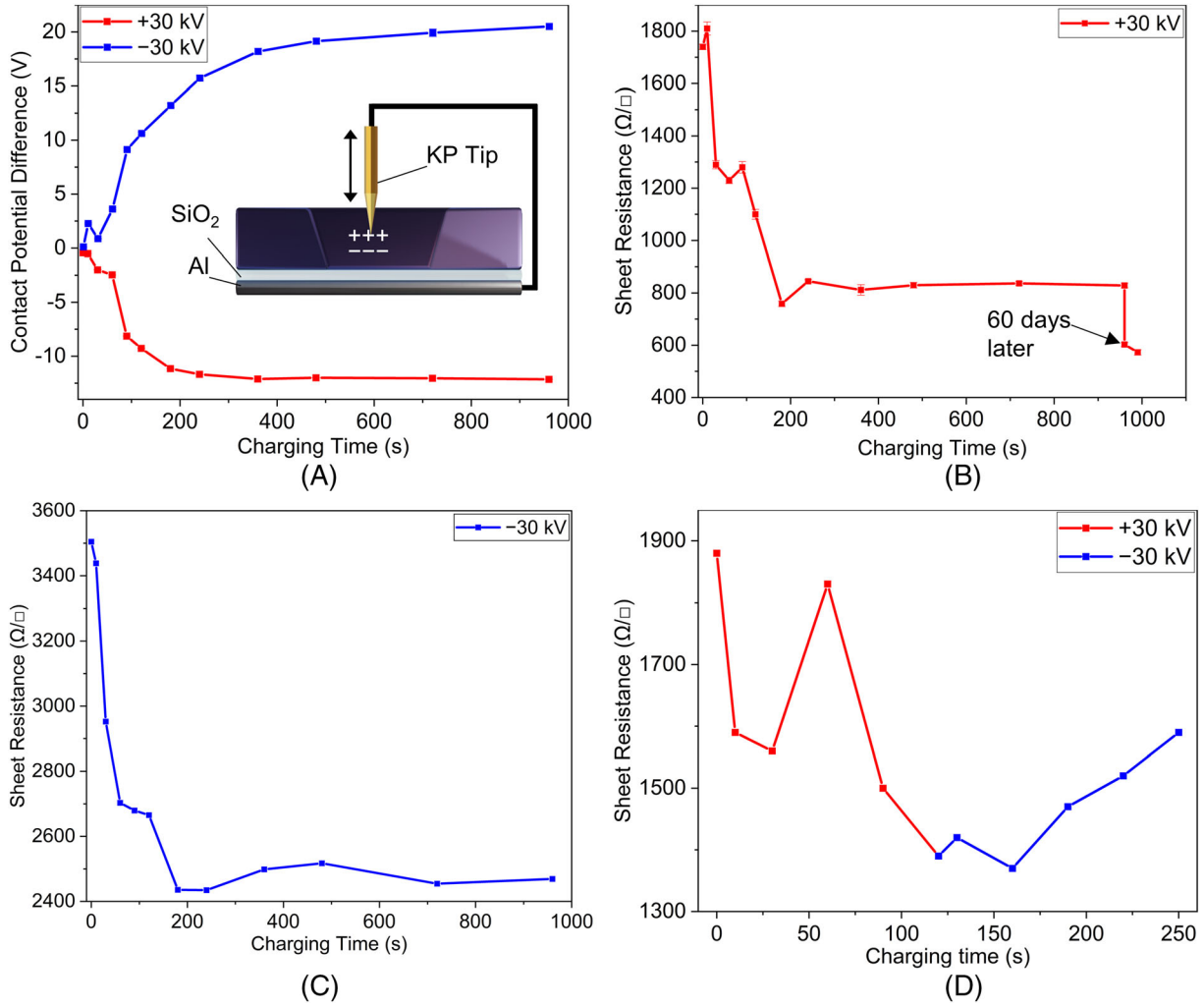

FIGURE 3 (A) Change in contact potential difference over time held under constant ±30 kV voltage, for a SiO_2 membrane measured by Kelvin probe microscopy. Inset: Kelvin probe microscopy measurement configuration. (B) Graphene sheet resistance over time held under constant +30 kV voltage. (C) Graphene sheet resistance over time held under constant −30 kV voltage. (D) Graphene sheet resistance as a function of time held under positive (red) and negative (blue) charge at ±30 kV. [Colour figure can be viewed at wileyonlinelibrary.com]

R_{sheet} measurements to be taken several minutes after each charging interval with confidence that the CPD will not have decayed substantially. The complete device was then manufactured including the graphene monolayer and contact electrodes and was subsequently charged under the corona discharge apparatus. Figure 3B shows how the R_{sheet} of graphene varied as the dielectric membrane was charged under +30 kV voltage over time. The initial R_{sheet} of ∼1740 Ω/□ is high for undoped CVD graphene. This is attributed to the difficulty of wet-transferring the graphene to substrates <1 cm^2, resulting in a large number of wrinkles, cracks and defects in the film. Figure 3C shows the R_{sheet} increase from 1740 to 1810 Ω/□ after 10 s of positive charging. This can be explained by the p-type nature of the undoped, as-transferred graphene. Graphene on SiO_2 is typically slightly p-doped because of the residual polymers left over from the transfer process, as well as interactions with moisture.[84] The 10 s of positive charging may have induced an n-type field effect large enough to reduce the p-type doping effect in the graphene, but insufficient for n-type behaviour. Increasing the amount of positive charge deposited on the membrane rapidly decreased the sheet resistance. It is assumed that the reduction of R_{sheet} observed is because of n-type electrostatic doping of the carriers in graphene by the positively charged dielectric substrate. In under 3 min, the R_{sheet} of graphene was reduced by ∼60% from 1810 to ∼759 Ω/□. After leaving this sample in a low-pressure nitrogenated chamber for 2 months, the sheet resistance decreased further, down to ∼607 Ω/□ (20% reduction). This is similar to the behaviour observed by Yu et al when investigating R_{sheet} reductions in ICD-charged dielectric nanolayers in inversion layer solar cells.[85] It is likely that the quasi-permanent field established causes further reductions of graphene's R_{sheet} over time. A device charged in the same way but stored in standard atmosphere and pressure, experienced a 2% (1910–1881 Ω/□) reduction in R_{sheet} after 2 months. For comparison, a set of uncharged devices experienced a 10%–15% increase R_{sheet} when held in standard laboratory conditions during the same time period, likely because of atmospheric

contamination, which reduces its mobility.[84,86,87] This indicates that the quasi-permanent field induced in the graphene counteracts the effect of atmospheric contamination from increasing R_{sheet}. When subjected to further positive charge deposition, the sheet resistance of the sample indicated in Figure 3B decreased further from 607 to ~573 Ω/□ in 30 s. No further reductions were observed as positive charging time increased. This is a combined reduction of R_{sheet} of 67% in the positively charged sample from the initial R_{sheet}. The relative change of R_{sheet} demonstrated in this novel doping technique is already approaching that of chemical doping, which typically reduces the R_{sheet} by 70%–80%.[31,88] Strategies for improving this technique beyond this work are described in Section 3.5.

Figure 3C shows how the R_{sheet} of graphene varied as the dielectric membrane was charged under −30 kV corona voltage over 16 min. The R_{sheet} decreases from 3.5 to 2.4 k Ω/□ after 3 min of negative charging time. This reduction in R_{sheet} is assumed to occur because of the p-type doping effect of the negatively-charged substrate, where holes are the majority carrier in graphene. As the graphene was already likely slightly p-doped, there was no increase in R_{sheet} as was observed with positive charging. The high initial R_{sheet} is due to processing difficulties resulting from using small substrates, as was the case in the positively charged sample. Because of the equal electron and hole mobilities in graphene,[89] both p- and n-type graphene TCEs can be developed using this technique. Figure 3D depicts the change in R_{sheet} of a graphene device subject to +30 kV for 2 min, followed by −30 kV for 2 min. Once again, the initial R_{sheet} was in the order of 1.9 kΩ/□ because of the faulty or defective graphene monolayers. Despite such high resistance, it is evident that the doping effect provided by the corona charge is reversible. The addition of negative electrostatic charge counteracted the n-type doping provided by initially deposited positive charges. This could enable precise conductivity tailoring for particular device applications, where both n- and p-type doping are required for better interconnection to active semiconductors.

Figure 4A depicts the variation in Hall carrier concentration and mobility of a graphene sheet as the membrane is charged with positive electrostatic charge over time. The initial charge carrier concentration of the graphene is high, at 1.56×10^{13} cm^{-2}, attributed to doping induced by remaining polymer residues.[84,90] The initial mobility was relatively low at ~213 cm^2/Vs. We attribute this low mobility to a high density of defects, wrinkles and cracks induced by the graphene wet transfer onto such small films, as well as scattering by polymer residues.[84,86,87] Such imperfections act as scattering centres that reduce the mean free path of the carriers and hence reduce mobility. The defects, wrinkles and cracks are likely to be the primary factors contributing to the high initial R_{sheet} observed in Figure 3A. The charge carrier concentration increases by nearly a factor of 3 after just 2 min of positive charge deposition, from 1.56×10^{13} to 4.35×10^{13} cm^{-2}. This indicates that deposition of positive charge on the dielectric film induces additional negative charge carriers in the graphene film. The carrier mobility decreases by just a factor of 2, from ~213 to ~104 cm^2/Vs. As the increase in n is greater than the decrease in μ, this results in a net decrease in R_{sheet}. It is noted, however, that the initially low mobility in our wet transferred films accounts for the high resistances initially observed, and it should be tackled to achieve competitive graphene. Unlike chemical doping, in ICD doping of graphene, the lattice is undisturbed and no additional scattering centres are induced from dopant atoms. This ensures that the mobility does not decrease significantly. This should allow for low FCA graphene TCEs in tandem cells.

Figure 4B depicts the variation in Hall carrier concentration and mobility of graphene as the membrane is charged with negative electrostatic charge over time. This device was first charged with positive charge, then negative charge. The carrier concentration initially decreases with applied negative charge concentration, indicating that this particular graphene film, unlike those in Figure 3, presented an initial level of n-type doping, which was compensated by the p-doping produced by negative charge on the SiO_2 membrane. Further negative

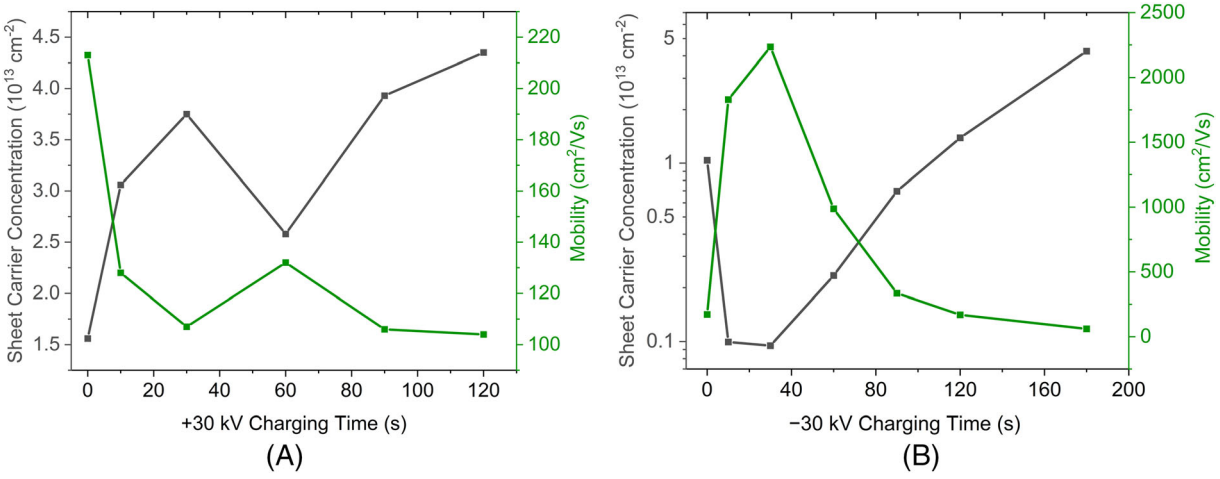

FIGURE 4 (A) Variation in graphene sheet carrier concentration and mobility as the SiO_2 membrane substrate is subjected to positive charge for 2 min. (B) Variation in graphene sheet carrier concentration and mobility as the SiO_2 membrane substrate is subjected to negative charge for 3 min. [Colour figure can be viewed at wileyonlinelibrary.com]

charging increased the carrier concentration by close to a factor of four from 1.04×10^{13} to 4.2×10^{13} cm^{-2}. The carrier mobility was observed to decrease by a factor of three from ~172 to ~60 cm^2/Vs after a complete 3 min of charge exposure, resulting in a net R_{sheet} reduction. Interestingly, the carrier mobility increases significantly from 172 to >2000 cm^2/Vs, whereas the carrier concentration decreased to ~10^{12} cm^{-2} during the initial 30 s of charge. Further exploration of this effect could allow for precise tailoring of the carrier concentration and mobility of graphene films in device applications.

3.2 | Raman spectroscopy

Defects in graphene are major scattering centres that can reduce mobility by reducing the mean free path of charge carriers. Raman spectroscopy allows the determination of whether the doping process introduced defects into the film, reducing mobility. The Raman spectrum of pristine graphene typically features two prominent peaks: the G peak at ~1580 cm^{-1}, which arises because of in-plane vibrations of sp^2 bonded carbon in the graphene lattice; and the 2D peak, at ~2690 cm^{-1}, which arises because of the breathing mode of sp^2 bonded carbon in hexagonal rings.[31,91] A third peak at ~1350 cm^{-1}, 'D', is present because of the defects in graphene.[31,91] The D/G intensity ratio is therefore used to provide an indication of the defect density in the film.

Figure 5 depicts the Raman spectrum of a device before and after positive electrostatic charging of the SiO_2 layer. The presence of the D peak in the uncharged device indicates that the initial high sheet resistance of 1740 Ω/□ was due to a high density of defects, reducing mobility, as discussed in Section 3.1. When charged, the D/G intensity ratio did not increase, indicating that no additional defects were induced by the electrostatic doping process. This contrasts with chemical doping techniques, which often induce additional defects in the graphene film because of lattice disruptions by dopant atoms.[25,65,72] Raman spectroscopy can indicate the degree and type of doping induced in graphene.[92–94] The slightly blueshifted G peak and decrease in full-width half maximum indicate that moderate doping has occurred.[92,94] The redshift of the 2D peak indicates that that doping is n-type.[92,94] Figure 6A,B depicts the G and 2D Raman shift of a device before and after negative electrostatic charging of the SiO_2 layer. There is a clear and distinct blueshift of the G and 2D peaks, indicative of p-doping. These findings are in line with those reported by Fates et al and Das et al where field effect modulation of the carrier concentration produces such changes to the G and 2D Raman spectrum peaks.[92,94]

3.3 | Optical characterisation

Figure 7A displays the experimental setup used to measure the transmission of the graphene devices on SiO_2 membranes. Figure 7B compares the transmission of 350–800 nm light between an undoped graphene film, a graphene film doped with a corona-charged SiO_2 membrane, ITO and IZO. The doping by corona-charged SiO_2 did not impact the >95% broadband transmissivity of graphene. This contrasts with most doping techniques that tend to cause transmissivity reductions because of the addition of dopant atoms.[25,65,72] The ability to alter the R_{sheet} of graphene rapidly and reversibly without impacting transmittance is significant, as it offers the potential to eliminate the challenging requirement to balance a trade-off between R_{sheet} and transmittance in TCEs.

Due to the limitations of in-house equipment, we were unable to measure the transmittance outside of the 350–800 nm window. Further work should include transmittance measurements across the entire AM1.5G spectrum before and after doping, to enable more meaningful comparisons between the optical properties of TCOs and ICD-doped graphene for tandem applications. The transmittance of undoped graphene remains broadband from 200 to 3000 nm, encompassing all light absorption within the AM1.5G spectrum.[95,96] If the ICD doping does not affect the transmittance of these regions, it

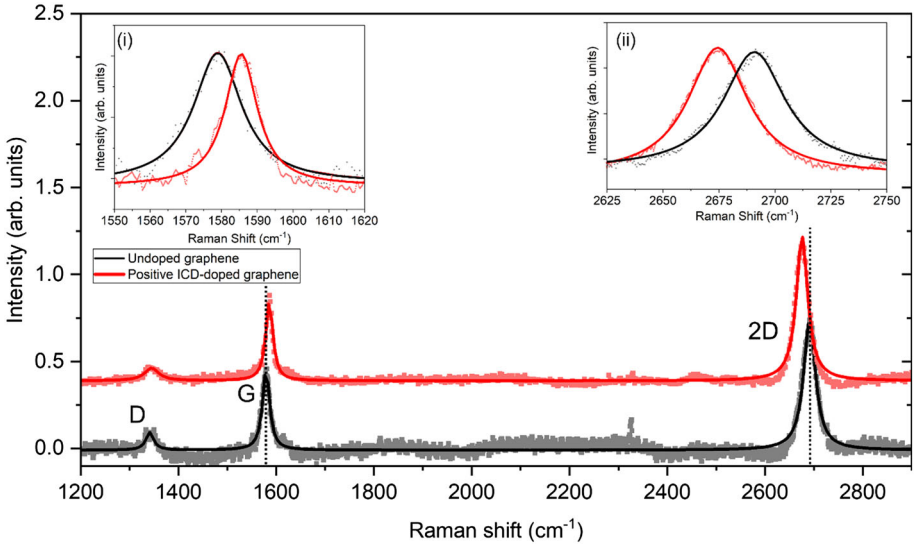

FIGURE 5 Raman intensity versus wavenumber for a graphene device with a positively charged SiO_2 substrate and an uncharged control. Data fit to a Lorentzian function. Inset (i): G peak Raman shift. Inset (ii): 2D peak Raman shift. [Colour figure can be viewed at wileyonlinelibrary.com]

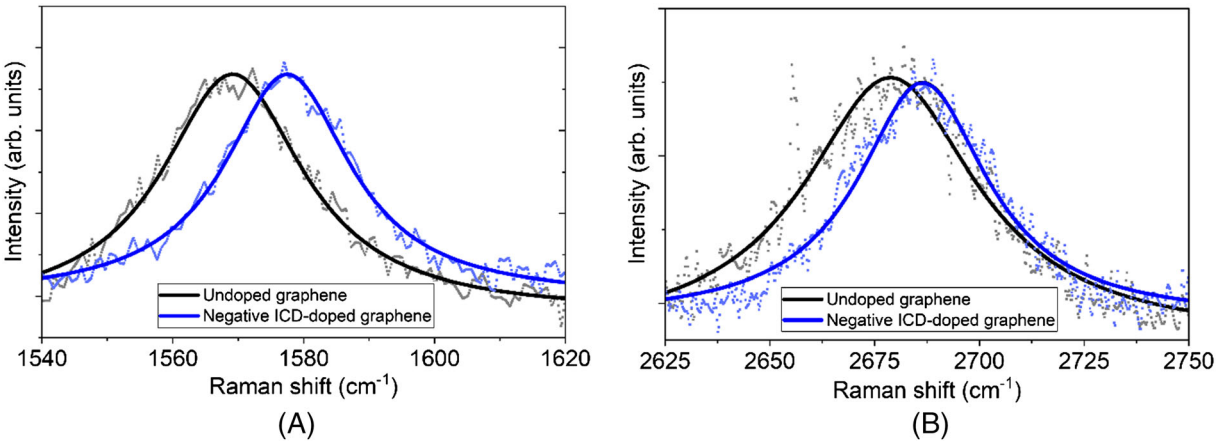

FIGURE 6 Raman intensity versus wavenumber for a graphene device with a negatively charged SiO_2 substrate and an uncharged control. (A) G peak Raman shift. (B) 2D peak Raman shift. [Colour figure can be viewed at wileyonlinelibrary.com]

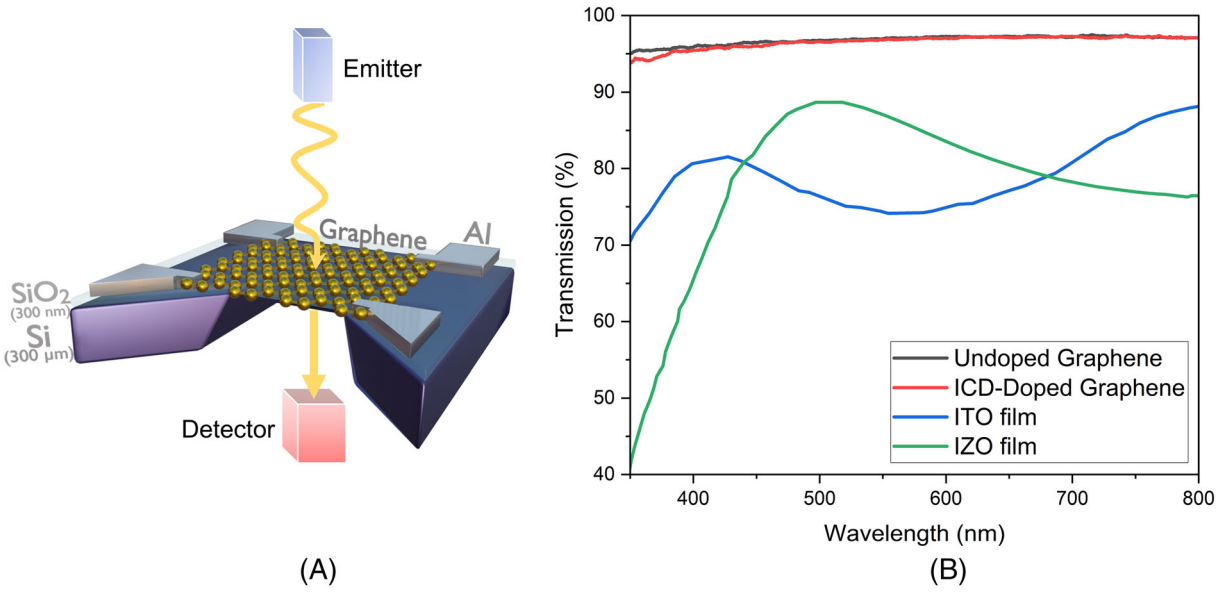

FIGURE 7 (A) Schematic of spectrophotometry transmission measurement of graphene film. (B) Transmission of undoped graphene, ion-charged dielectric (ICD)-doped graphene, a typical indium tin oxide (ITO) film (ITO data[65]) and a typical indium zinc oxide (IZO) film (IZO data[66]). [Colour figure can be viewed at wileyonlinelibrary.com]

opens up the possibility for a highly transmissive TCE for tandem cell applications.

3.4 | Target R_{sheet} for ICD-doped graphene TCEs for two-terminal monolithic perovskite/silicon tandem solar cells

The transmittance of graphene is uniquely broadband, offering optical advantages over ITO and IZO alternatives. In this work, we have shown experimental data indicating that ICD-doping of graphene does not impact its transmittance. Therefore, it is not expected that ICD-doped graphene would require an R_{sheet} as low as that of ITO or IZO to remain competitive for application as a TCE in tandem cells. To evaluate the R_{sheet} required for a graphene TCE to match the performance of an ITO or IZO film, we have modelled the ultimate tandem cell performance following the approach recently published by Anand et al.[82] In this model, the theoretical performance of the cell is calculated for variations in the transmittance and sheet resistance of the TCE. This allows a comparison between the theoretical efficiency achieved in tandem cells when they incorporate different TCEs. Anand et al's work uses a detailed balance calculation to obtain the maximum power conversion efficiency of a single-junction solar cell with a given band gap, absorbing the AM1.5G spectrum. In this work, such detailed balance calculation is extended to the absorption and collection taking place in a two-terminal monolithic tandem device

with silicon as the bottom cell. This is the most suitable device to focus on when drawing conclusions relevant to perovskite-silicon tandem solar cells. Figure 8 illustrates the unit domain used for the calculation, where two possible architectures are proposed. In the first architecture (Figure 8A), a front TCE is placed on the surface of the perovskite semiconductor, collecting current and driving it to localised front metal contacts. The current flow is assumed to be completely vertical because of the presence of a suitable optoelectronic link or an interconnection layer. This is often referred to as the recombination layer, but here, it is generalised to a layer(s) fulfilling both conduction and optical coupling functions. When vertical current flow is desired in the silicon absorber, a second TCE must be present at the rear surface as is typical in SHJ technology. A possible second approach (Figure 8B) uses surface doping in the silicon sub-cell to enable flow of charge carriers to a local contact both at the front and rear. This architecture would reflect the use of a different silicon bottom cell, for example, a passivated emitter and rear cell PERC or a tunnelling oxide passivating contact (TOPCon) architecture. Here, the rear TCE is present on top of the optoelectronic link to indicate that the current collected in the perovskite semiconductor must be conducted to the local contact at the front of the silicon sub-cell. Such a design was originally used to produce perovskite/silicon tandem cells,[23] making it highly relevant to the current large-scale production of solar panels. For both cases in Figure 8A,B, each TCE accounts for one additional series resistance such that the effective series resistance must include two contributions, as detailed in Section S6, Supplementary Material. Optically, the case in Figure 8A is more favourable as front light only passes through a single TCE. Accordingly, here, we have modelled the ultimate theoretical efficiency assuming the case of Figure 8A. This is used to determine the R_{sheet} required for a graphene TCE with broadband transmittance to negligibly contribute to electrical losses when implemented in such tandem cell architectures.

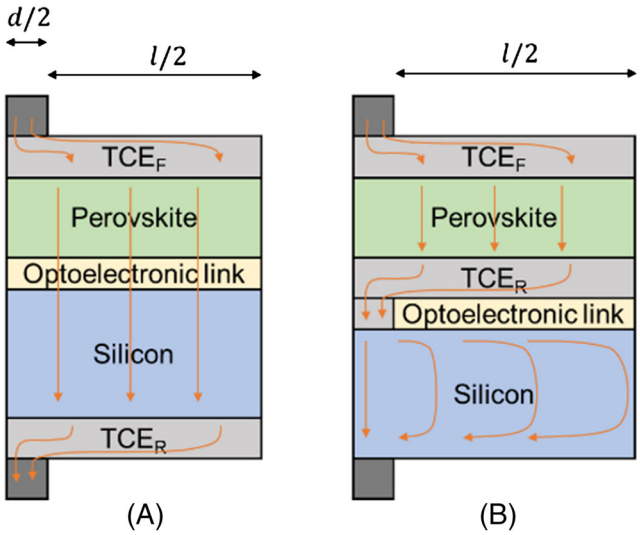

FIGURE 8 Unit domains of two-terminal tandem solar cells with *d* representing the finger width and *l* the finger pitch. (A) Lateral view of two-terminal tandem with front and rear transparent conducting electrode (TCE) for bifacial configuration. (B) Lateral view of two-terminal tandem solar cell with front TCE and TCE between subcells. [Colour figure can be viewed at wileyonlinelibrary.com]

Figure 9 shows the results of the model when applied to several potential TCEs. Here, a contour map of the upper efficiency limit for a two-terminal perovskite/silicon tandem is illustrated as a function of uniform spectral transmittance (280–1100 nm), using a 1 Sun weighted averaging to account for wavelength dependence. The y-axis of Figure 9 is the 'Weighted Average Transmittance' (WAT) from 85%–100%, calculated across the AM1.5G using the transfer-matrix method (see Section S7, Supplementary Material). Based on our model, the optimum thickness for films of ITO, IO:H, tungsten-doped indium oxide (IWO), IZO and IZRO films is ≈40 nm. Although the R_{sheet} is higher relative to the typical 100 nm case, the WAT increases significantly, resulting in an optimised balance of properties for high efficiencies in tandems. As thickness increases beyond 40 nm, the WAT decreases significantly, resulting in a reduction in efficiencies. ITO films of thickness 40 nm offer maximum efficiencies ≈41%, whether lightly or heavily doped. This is in stark contrast to a typical 100 nm film, which has a maximum efficiency of <40%. IZO films of 40 nm offer efficiencies >41% because of their high mobility and low parasitic absorption. IWO and IO:H films of 40 nm are both promising TCOs that offer maximum efficiencies ~$1\%_{abs}$ greater than that of ITO, at ~42% each. IZRO films of 40 nm are the most promising TCO considered here, offering efficiencies approaching 43%.

The typical target sheet resistance for TCEs in optoelectronics is ≈10 Ω/□. Isolating this value on the x-axis, we can see that increasing the transmittance impacts the maximum efficiency significantly. At 10 Ω/□, increasing transmittance by $7\%_{rel}$ from 90% to 97% increases the efficiency potential from 40.5% to >44%. At 97% transmittance, reducing the R_{sheet} by $500\%_{rel}$ from 50 to 10 Ω/□ would have a negligible impact on maximum efficiency. In this work, the graphene displays broadband transmittance >95%. This results in a maximum efficiency potential of >42% for R_{sheet} less than ≈573 Ω/□. Optimizing the performance of ICD-doped graphene to have a transmittance of 97.5% and an R_{sheet} ≈ 50 Ω/□ could facilitate maximum power conversion efficiencies as high as 44%. Thus, if graphene could be harnessed as a TCE for two-terminal perovskite/silicon tandem cells, the strict requirement on R_{sheet} could be significantly relaxed, as well as providing increasing sustainability by eliminating indium from the cell. In the next section, we shall discuss strategies to realistically achieve a reduction in R_{sheet} in ICD-doped graphene from ≈600 to ≈50 Ω/□, to practically enable the predictions of the model and its feasibility to integrate into a tandem cell device.

3.5 | Discussion

The proof-of-principle graphene TCE device proposed in this work exhibited a decrease in R_{sheet} of nearly 70% through the corona discharge induction of an electrostatic field in an interfacing SiO_2 thin film. This occurs as the Fermi level of 2D materials such as graphene is easily disturbed under application of an electric field.[73] Using theoretical modelling, we demonstrated that a maximum perovskite/silicon

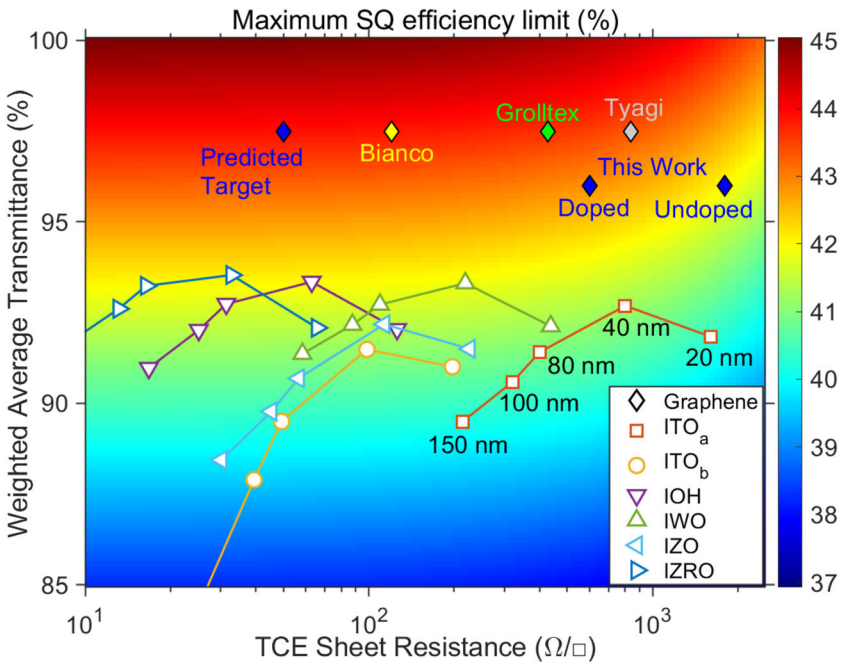

FIGURE 9 Plot of the maximum efficiency that can be obtained using a top perovskite cell of $E_g = 1.73$ eV, two transparent conducting electrodes (TCEs) (one front and one rear), with a variation in sheet resistance and integrated transmittance across the air-mass 1.5 global (AM1.5G) spectrum. Tyagi (graphene),[97] *Grolltex* (graphene),[98] Bianco (graphene),[31] indium tin oxide $(ITO)_a$ (lightly doped, $n = 6.5 \times 10^{19}$ cm^{-3}),[69] ITO_b (heavily doped, $n = 6.1 \times 10^{20}$ cm^{-3}),[69] hydrogen-doped indium oxide (IO:H),[99] tungsten-doped indium oxide (IWO),[100] IZO[66] and Zirconium oxide doped In_2O_3 (IZRO).[26] [Colour figure can be viewed at wileyonlinelibrary.com]

tandem efficiency of up to 44% could be realised if R_{sheet} < 50 Ω/□ could be obtained in graphene without impacting its transmittance. In this work, despite not impacting transmittance, the measured R_{sheet} of the ICD-doped graphene was ≈573 Ω/□, an order of magnitude above our target R_{sheet} of <50 Ω/□. Fortunately, there are several ways to improve the ICD doping of graphene that could facilitate R_{sheet} < 50 Ω/□. A key limitation of this work was the small 0.5 × 0.5 cm^2 size of the substrates used. It is challenging to carry out the wet transfer process on substrates <1 cm^2 because of the increased manual dexterity required. Transferring the small 0.4 × 0.4 cm^2 sheet to this substrate likely subjected the graphene to additional strain, resulting in the formation of additional wrinkles, cracks and holes. The presence of such deformations is supported by the prominent D peaks in its Raman spectra, which indicate a high density of defects. This high defect density resulted in a lower mobility and R_{sheet} than is typical of monolayer CVD graphene. For perovskite/silicon tandem cell applications, a larger area sheet with a lower R_{sheet} can be transferred. For example, monolayer CVD graphene films on Si/SiO_2 with undoped R_{sheet} 430 ± 50 Ω/□ in areas up to 200 mm are now commercially available,[98] and graphene transfer on A4-sized sheets has now been demonstrated.[101,102] As corona charge deposition and dielectric synthesis can occur on wafer-scale dimensions, this demonstrates the feasibility of producing ICD-doped graphene on industrially relevant scales. This shows that by ICD-doping such high-quality CVD graphene sheets, R_{sheet} < 150 Ω/□ with transmittance >95% in graphene on dimensions large enough for typical solar cells could be facilitated. This assumes that with a maximum CPD of about −12 V, as measured in this work, the same relative reduction in R_{sheet} would occur because of an increase of carrier concentration by a factor of three.

A higher charge concentration can be deposited on the film, providing a stronger electrostatic doping effect. We have shown that a maximum CPD of about −80 V is attainable on these membranes when the membrane is positively charged from the top side (see Figures S2 and S3, Section S3, Supplementary Material). This is a near-sevenfold increase in CPD as compared with the films used in this work. CPD of this magnitude was not attained when charged from the rear, because of the screening of corona charge by the 100 nm SiO_2 layer on the Si support (see Section S3, Supplementary Material). This 100 nm SiO_2 layer on the Si support is closer to the discharge electrode, resulting in significant charge build-up on the support, which repelled the deposition of additional ionic charge. However, in a practical perovskite/silicon tandem device, this screening effect would not occur as the distance between the discharge electrode and the target dielectric would be the minimum distance. In such cases, a uniform thin film dielectric would be deposited and embedded with a concentration of charge, leading to the possibility of much larger area TCEs with low sheet resistance. This would also avoid the intrinsic difficulties of working with small, suspended SiO_2 membranes. Therefore, we expect that a reduction in sheet resistance from 150 to 50 Ω/□ is practically achievable by optimising the charge deposition conditions.

The maximum CPD attainable on a 300 nm SiO_2 membrane should exceed 100 V and is only limited by its dielectric breakdown strength.[103,104] In a practical device, the membrane would not be suspended but instead incorporated in an optoelectronic device stack. We demonstrated that the maximum CPD attainable on SiO_2 on substrates used in this work was −100 V when supported by Si, reached after just 3 min of positive charging (see Figure S4, Supplementary Material). This demonstrates a significant increase in doping potential beyond what has been demonstrated in this work. With improved dielectric synthesis techniques, the amount of charge deposited on the film can be increased to meet this limit. Such improvements should enable sheet resistances <50 Ω/□ to be

obtained. Using Bonilla et al's method to permanently embed large concentrations of charge in thin films of SiO_2 with corona charge and solid-state alkali ions,[77,78] this graphene doping technique could be stabilised on commercial timescales. Electrostatic ICD doping of graphene is also applicable to other materials that store corona charge. An ionic charge concentration comparable to that used for graphene doping in this work can be deposited on SiN_x dielectric membranes with a thickness of 100 nm, as shown in Supplementary Material Section S3, Figure S5. The thickness can be reduced significantly without compromising charge deposition on the film, as the amount of charge that can be deposited on a dielectric only depends on the dielectric constant and dielectric strength of the material (see Supplementary Material Section S5). This provides opportunities for varied device requirements and potential combination of ICD-doped TCEs with anti-reflection layers. For example, a charged SiN_x layer of 75 nm thickness could be used as an anti-reflection layer, while also electrostatically doping the graphene which is interfaced with the perovskite HTL or ETL at the front of a perovskite/silicon tandem.

We envision device integration involving the replacement of a conventional TCE layer in a tandem cell stack with an ICD placed adjacent to a monolayer graphene sheet. In a two-terminal monolithic perovskite/silicon tandem, this ICD-doped graphene layer could be placed at the top of the perovskite subcell and at the rear of the silicon bottom cell. Note that such a TCE could not replace the recombination layer in a two-terminal tandem, as doing so would impede vertical charge transport. In a four-terminal mechanically-stacked perovskite/silicon tandem, such an ICD-doped graphene layer could also be positioned under the perovskite or on top of the silicon subcells. In all cases, the graphene layer would be oriented to the absorber to collect charge carriers, as the dielectric layer would impede vertical charge transport. Because of the compatibility of graphene with several HTL and ETL materials and the ambipolarity of the doping technique, ICD-doped graphene could be integrated in either p-i-n or n-i-p perovskite cell configuration, offering wide adaptability for different device processing constraints.[58] In a solar cell device, the metal electrode could be positioned in between the ICD and conductive graphene or the metal could be laser-fired through the dielectric to form an electrical contact with the graphene. Several technical limitations remain before such an electrode could be fabricated at industrially relevant speeds. The production of CVD graphene is currently relatively slow compared with TCOs, typically requiring separate steps for production and transfer to the target device.[105] High-quality, large-area CVD graphene can be transferred to flexible substrates via roll-to-roll techniques, at speeds up to 500 mm/min,[32,105,106] and transferred to rigid substrates within 15 min.[107] The fabrication and charging of the dielectric layer would involve an additional step. Whereas engineering challenges remain for ICD-doped graphene TCEs to match the industrial speeds of TCOs, graphene fabrication and transfer benefits from being less energy intensive than fabricating indium-based TCOs and is inherently less expensive because of not requiring scarce materials.[46]

4 | CONCLUSION

In this work, we present results detailing a novel graphene doping technique that could enable a promising TCE compatible with tandem cells. This technique can lead to the production of graphene-based TCEs with optical and electrical properties competitive with ITO and IZO. Electrostatic charge deposition on a supporting dielectric substrate is used to tune the conductivity of graphene. We observe that the sheet resistance of graphene can be reduced by 60% in just 3 miutes of positive electrostatic charging of the underlying dielectric film. This technique does not impact transmittance, does not disturb the graphene lattice and can be stabilised on commercially relevant timescales. The doping is tuneable and readily reversible in less than 5 min, so that it can be tailored to different device applications. Using theoretical modelling, we showed that high-quality graphene doped with our novel technique could enable efficiencies up to 44% if $R_{sheet} < 50\ \Omega/\square$ can be obtained without impacting transmittance. This is a significant increase in efficiency potential as compared with current alternatives while also eliminating the unsustainable use of indium in next-generation solar cells.

This technique and material are compatible with tandem solar cells and aim to provide a low-cost, sustainable alternative to indium-based TCEs for photovoltaic capacity at terawatt-scales. Such advantages could markedly improve cell efficiencies and price-performance ratios. The ease and rapid processing of this technique could enable faster, more economically viable and energy-efficient tandem cell production. This can facilitate a more accelerated uptake of renewable energy sources in the face of the current climate crisis.

ACKNOWLEDGEMENTS

All the authors are thankful to Radka Chakalova for assistance in clean-room processing. Ruy S. Bonilla was supported by the Royal Academy of Engineering under the Research Fellowship scheme. This work was supported by the UK Engineering and Physical Sciences Research Council grant number EP/V038605/1 and by the John Fell Fund, University of Oxford. For the purpose of Open Access, the author has applied a CC BY public copyright licence to any Author Accepted Manuscript (AAM) version arising from this submission.

DATA AVAILABILITY STATEMENT

All data created during this research and published in this article is openly available from the Oxford University Research Archive and can be downloaded free of charge from http://ora.ox.ac.uk.

ORCID

John O'Sullivan https://orcid.org/0000-0002-4136-0067

REFERENCES

1. Niewelt T, Steinhauser B, Richter A, et al. Reassessment of the intrinsic bulk recombination in crystalline silicon. *Sol Energy Mater Sol Cells*. 2022;235:111467. doi:10.1016/j.solmat.2021.111467
2. Yoshikawa K, Kawasaki H, Yoshida W, et al. Silicon heterojunction solar cell with interdigitated back contacts for a photoconversion

efficiency over 26%. *Nat Energy*. 2017;2(5):1-8. doi:10.1038/nenergy.2017.32
3. Lin H, Yang M, Ru X, et al. Silicon heterojunction solar cells with up to 26.81% efficiency achieved by electrically optimized nanocrystalline-silicon hole contact layers. *Nat Energy*. 2023;2023(8):1-11. doi:10.1038/s41560-023-01255-2
4. Shen H, Walter D, Wu Y, et al. Monolithic perovskite/Si tandem solar cells: pathways to over 30% efficiency. *Adv Energy Mater*. 2020;10(13):1902840. doi:10.1002/AENM.201902840
5. Al-Ashouri A, Köhnen E, Li B, et al. Monolithic perovskite/silicon tandem solar cell with >29% efficiency by enhanced hole extraction. *Science*. 2020;370(6522):1300-1309. doi:10.1126/SCIENCE.ABD4016/SUPPL_FILE/ABD4016_AL-ASHOURI_SM.PDF
6. Yu Z, Leilaeioun M, Holman Z. Selecting tandem partners for silicon solar cells. *Nat Energy*. 2016;1(11):16137. doi:10.1038/nenergy.2016.137
7. Futscher MH, Ehrler B. Modeling the performance limitations and prospects of perovskite/Si tandem solar cells under realistic operating conditions. *ACS Energy Lett*. 2017;2(9):2089-2095. doi:10.1021/ACSENERGYLETT.7B00596/SUPPL_FILE/NZ7B00596_SI_001.PDF
8. Futscher MH, Ehrler B. Efficiency limit of perovskite/Si tandem solar cells. *ACS Energy Lett*. 2016;1(4):863-868. doi:10.1021/acsenergylett.6b00405
9. De Wolf S, Holovsky J, Moon S-J, et al. Organometallic halide perovskites: sharp optical absorption edge and its relation to photovoltaic performance. *J Phys Chem Lett*. 2014;5(6):1035-1039. doi:10.1021/jz500279b
10. Zhao H, Han Y, Xu Z, et al. A novel anion doping for stable CsPbI2Br perovskite solar cells with an efficiency of 15.56% and an open circuit voltage of 1.30 V. *Adv Energy Mater*. 2019;9(40):1902279. doi:10.1002/aenm.201902279
11. Manzoor S, Häusele J, Bush KA, Yu ZJ, McGehee MD, Holman ZC. Current-matching in two-terminal perovskite/silicon tandems employing wide-bandgap perovskites and varying light-management schemes. In: *2018 IEEE 7th World Conference on Photovoltaic Energy Conversion (WCPEC) (A Joint Conference of 45th IEEE PVSC, 28th PVSEC & 34th EU PVSEC), Waikoloa, HI, USA*:220-223. doi:10.1109/PVSC.2018.8547757
12. Duan W, Lambertz A, Bittkau K, et al. A route towards high-efficiency silicon heterojunction solar cells. *Prog Photovoltaics Res Appl*. 2022;30(4):384-392. doi:10.1002/PIP.3493
13. Morales-Masis M, De Wolf S, Woods-Robinson R, Ager JW, Ballif C. Transparent electrodes for efficient optoelectronics. *Adv Electron Mater*. 2017;3(5):1600529. doi:10.1002/AELM.201600529
14. Granqvist CG. Transparent conductors as solar energy materials: a panoramic review. *Sol Energy Mater Sol Cells*. 2007;91(17):1529-1598. doi:10.1016/j.solmat.2007.04.031
15. Chopra KL, Major S, Pandya DK. Transparent conductors-A status review. In: *Thin solid films*. Vol.102. Elsevier; 1983:1-46. doi:10.1016/0040-6090(83)90256-0
16. Jacobs DA, Catchpole KR, Beck FJ, White TP. A re-evaluation of transparent conductor requirements for thin-film solar cells. *J Mater Chem A*. 2016;4(12):4490-4496. doi:10.1039/c6ta01670g
17. Rowell MW, McGehee MD. Transparent electrode requirements for thin film solar cell modules. *Energ Environ Sci*. 2011;4(1):131-134. doi:10.1039/c0ee00373e
18. Zhang Y, Kim M, Wang L, Verlinden P, Hallam B. Design considerations for multi-terawatt scale manufacturing of existing and future photovoltaic technologies: challenges and opportunities related to silver, indium and bismuth consumption. *Energ Environ Sci*. 2021;14(11):5587-5610. doi:10.1039/D1EE01814K
19. Wang L, Zhang Y, Kim M, et al. Sustainability evaluations on material consumption for terawatt-scale manufacturing of silicon-based tandem solar cells. *Prog Photovoltaics Res Appl*. 2023:1-13. doi:10.1002/PIP.3687
20. Emmott CJM, Urbina A, Nelson J. Environmental and economic assessment of ITO-free electrodes for organic solar cells. *Sol Energy Mater Sol Cells*. 2012;97:14-21. doi:10.1016/J.SOLMAT.2011.09.024
21. Todorov T, Gunawan O, Guha S. A road towards 25% efficiency and beyond: perovskite tandem solar cells. *Mol Syst Des Eng*. 2016;1(4):370-376. doi:10.1039/C6ME00041J
22. Jacobs DA, Langenhorst M, Sahli F, et al. Light management: a key concept in high-efficiency perovskite/silicon tandem photovoltaics. *J Phys Chem Lett*. 2019;10(11):3159-3170. doi:10.1021/acs.jpclett.8b03721
23. Wu Y, Yan D, Peng J, et al. Monolithic perovskite/silicon-homojunction tandem solar cell with over 22% efficiency. *Energ Environ Sci*. 2017;10(11):2472-2479. doi:10.1039/c7ee02288c
24. Fu F, Li J, Yang TCJ, et al. Monolithic perovskite-silicon tandem solar cells: from the lab to fab? *Adv Mater*. 2022;34(24):2106540. doi:10.1002/ADMA.202106540
25. Brunin G, Ricci F, Ha VA, Rignanese GM, Hautier G. Transparent conducting materials discovery using high-throughput computing. *npj Comput Mater*. 2019;5:1-13. doi:10.1038/s41524-019-0200-5
26. Aydin E, de Bastiani M, Yang X, et al. Zr-doped indium oxide (IZRO) transparent electrodes for perovskite-based tandem solar cells. *Adv Funct Mater*. 2019;29(25):1901741. doi:10.1002/adfm.201901741
27. Wang D, Wright M, Elumalai NK, Uddin A. Stability of perovskite solar cells. *Sol Energy Mater Sol Cells*. 2016;147:255-275. doi:10.1016/J.SOLMAT.2015.12.025
28. Morales-Vilches AB, Cruz A, Pingel S, et al. ITO-free silicon heterojunction solar cells with ZnO:Al/SiO2 front electrodes reaching a conversion efficiency of 23%. *IEEE J Photovoltaics*. 2019;9(1):34-39. doi:10.1109/JPHOTOV.2018.2873307
29. Kim H, Piqué A, Horwitz JS, et al. Indium tin oxide thin films for organic light-emitting devices. *Appl Phys Lett*. 1999;74(23):3444-3446. doi:10.1063/1.124122
30. Haschke J, Lemerle R, Aissa B, et al. Annealing of silicon heterojunction solar cells: interplay of solar cell and indium tin oxide properties. *IEEE J Photovoltaics*. 2019;9(5):1202-1207. doi:10.1109/JPHOTOV.2019.2924389
31. Bianco GV, Sacchetti A, Milella A, et al. Extraordinary low sheet resistance of CVD graphene by thionyl chloride chemical doping. *Carbon*. 2020;170:75-84. doi:10.1016/j.carbon.2020.07.038
32. Bae S, Kim H, Lee Y, et al. Roll-to-roll production of 30-inch graphene films for transparent electrodes. *Nat Nanotechnol*. 2010;5(8):574-578. doi:10.1038/nnano.2010.132
33. Khusayfan NM, El-Nahass MM. Study of structure and electro-optical characteristics of indium tin oxide thin films. *Adv Condens Matter Phys*. 2013;2013:1-8. doi:10.1155/2013/408182
34. Minami T. Transparent conducting oxide semiconductors for transparent electrodes. *Semicond Sci Technol*. 2005;20(4):S35-S44. doi:10.1088/0268-1242/20/4/004
35. Kanai Y. Electrical properties of indium-tin-oxide single crystals. *Jpn J Appl Phys*. 1984;23(1):12-14. doi:10.1143/JJAP.23.L12
36. Ellmer K, Mientus R. Carrier transport in polycrystalline transparent conductive oxides: a comparative study of zinc oxide and indium oxide. *Thin Solid Films*. 2008;516(14):4620-4627. doi:10.1016/j.tsf.2007.05.084
37. Kim YC, Jeong H-J, Kim S-T, et al. Luminescent down-shifting $CsPbBr_3$ perovskite nanocrystals for flexible Cu(In,Ga)Se_2 solar cells. *Nanoscale*. 2020;12(2):558-562. doi:10.1039/C9NR06041C
38. Kothandaraman RK, Jiang Y, Feurer T, Tiwari AN, Fu F. Near-infrared-transparent perovskite solar cells and perovskite-based tandem photovoltaics. *Small Methods*. 2020;4(10):2000395. doi:10.1002/SMTD.202000395
39. Chen B, Baek SW, Hou Y, et al. Enhanced optical path and electron diffusion length enable high-efficiency perovskite tandems. *Nat Commun*. 2020;11(1):1257. doi:10.1038/s41467-020-15077-3

40. Kobayashi E, Watabe Y, Yamamoto T, Yamada Y. Cerium oxide and hydrogen co-doped indium oxide films for high-efficiency silicon heterojunction solar cells. *Sol Energy Mater Sol Cells*. 2016;149:75-80. doi:10.1016/J.SOLMAT.2016.01.005
41. Filipič M, Löper P, Niesen B, et al. $CH_3NH_3PbI_3$ perovskite/silicon tandem solar cells: characterization based optical simulations. *Opt Express*. 2015;23(7):A263-A278. doi:10.1364/oe.23.00a263
42. Bett AJ, Winkler KM, Bivour M, et al. Semi-transparent perovskite solar cells with ITO directly sputtered on Spiro-OMeTAD for tandem applications. *ACS Appl Mater Interfaces*. 2019;11(49):45796-45804. doi:10.1021/ACSAMI.9B17241/ASSET/IMAGES/LARGE/AM9B17241_0005.JPEG
43. Smirnov Y, Repecaud PA, Tutsch L, et al. Wafer-scale pulsed laser deposition of ITO for solar cells: reduced damage vs. interfacial resistance. *Mater Adv*. 2022;3(8):3469-3478. doi:10.1039/D1MA01225H
44. Aydin E, Altinkaya C, Smirnov Y, et al. Sputtered transparent electrodes for optoelectronic devices: induced damage and mitigation strategies. *Matter*. 2021;4(11):3549-3584. doi:10.1016/J.MATT.2021.09.021
45. Rosli NN, Ibrahim MA, Ahmad Ludin N, Mat Teridi MA, Sopian K. A review of graphene based transparent conducting films for use in solar photovoltaic applications. In: *Renewable and sustainable energy reviews*. Vol.99. Elsevier Ltd; 2019:83-99. doi:10.1016/j.rser.2018.09.011
46. Arvidsson R, Kushnir D, Molander S, Sandén BA. Energy and resource use assessment of graphene as a substitute for indium tin oxide in transparent electrodes. *J Clean Prod*. 2016;132:289-297. doi:10.1016/j.jclepro.2015.04.076
47. Kim YY, Yang TY, Suhonen R, et al. Roll-to-roll gravure-printed flexible perovskite solar cells using eco-friendly antisolvent bathing with wide processing window. *Nat Commun*. 2020;11(1):1-11. doi:10.1038/s41467-020-18940-5
48. Lang F, Gluba MA, Albrecht S, et al. Perovskite solar cells with large-area CVD-graphene for tandem solar cells. *J Phys Chem Lett*. 2015;6(14):2745-2750. doi:10.1021/acs.jpclett.5b01177
49. Lang F, Gluba MA, Albrecht S, et al. In situ graphene doping as a route toward efficient perovskite tandem solar cells. *Phys Status Solidi*. 2016;213(7):1989-1996. doi:10.1002/PSSA.201532944
50. Liu Z, You P, Xie C, Tang G, Yan F. Ultrathin and flexible perovskite solar cells with graphene transparent electrodes. *Nano Energy*. 2016;28:151-157. doi:10.1016/j.nanoen.2016.08.038
51. You P, Liu Z, Tai Q, Liu S, Yan F. Efficient semitransparent perovskite solar cells with graphene electrodes. *Adv Mater*. 2015;27(24):3632-3638. doi:10.1002/ADMA.201501145
52. Sung H, Ahn N, Jang MS, et al. Transparent conductive oxide-free graphene-based perovskite solar cells with over 17% efficiency. *Adv Energy Mater*. 2016;6(3):1501873. doi:10.1002/AENM.201501873
53. Tran VD, Pammi SVN, Park BJ, Han Y, Jeon C, Yoon SG. Transfer-free graphene electrodes for super-flexible and semi-transparent perovskite solar cells fabricated under ambient air. *Nano Energy*. 2019;65:104018. doi:10.1016/J.NANOEN.2019.104018
54. Yoon J, Sung H, Lee G, et al. Superflexible, high-efficiency perovskite solar cells utilizing graphene electrodes: towards future foldable power sources. *Energ Environ Sci*. 2017;10(1):337-345. doi:10.1039/c6ee02650h
55. Heo JH, Shin DH, Jang MH, Lee ML, Kang MG, Im SH. Highly flexible, high-performance perovskite solar cells with adhesion promoted AuCl3-doped graphene electrodes. *J Mater Chem A*. 2017;5(40):21146-21152. doi:10.1039/C7TA06465A
56. Yan K, Wei Z, Li J, et al. High-performance graphene-based hole conductor-free perovskite solar cells: Schottky junction enhanced hole extraction and electron blocking. *Small*. 2015;11(19):2269-2274. doi:10.1002/SMLL.201403348
57. Bouclé J, Herlin-Boime N. The benefits of graphene for hybrid perovskite solar cells. *Synth Met*. 2016;222:3-16. doi:10.1016/J.SYNTHMET.2016.03.030
58. Choi J-M, Han J, Yoon J, Kim S, Jeon I, Maruyama S. Overview and outlook on graphene and carbon nanotubes in perovskite photovoltaics from single-junction to tandem applications. *Adv Funct Mater*. 2022;32(42):2204594. doi:10.1002/ADFM.202204594
59. Fernández S, Boscá A, Pedrós J, et al. Advanced graphene-based transparent conductive electrodes for photovoltaic applications. *Micromachines*. 2019;10(6):402. doi:10.3390/MI10060402
60. Lancellotti L, Bobeico E, Della Noce M, et al. Graphene as non conventional transparent conductive electrode in silicon heterojunction solar cells. *Appl Surf Sci*. 2020;525:146443. doi:10.1016/J.APSUSC.2020.146443
61. Torres I, Fernández S, Fernández-Vallejo M, Arnedo I, Gandía JJ. Graphene-based electrodes for silicon heterojunction solar cell technology. *Dent Mater*. 2021;14(17):4833. doi:10.3390/MA14174833
62. Shen JJ. Recently-explored top electrode materials for transparent organic solar cells. *Synth Met*. 2021;271:116582. doi:10.1016/J.SYNTHMET.2020.116582
63. Zhu SE, Yuan S, Janssen GCAM. Optical transmittance of multilayer graphene. *EPL*. 2014;108(1):17007. doi:10.1209/0295-5075/108/17007
64. Nair RR, Blake P, Grigorenko AN, et al. Fine structure constant defines visual transparency of graphene. *Science*. 2008;320(5881):1308. doi:10.1126/science.1156965
65. Wang J, Ma F, Liang W, Wang R, Sun M. Optical, photonic and optoelectronic properties of graphene, h-NB and their hybrid materials. *Nanophotonics*. 2017;6(5):943-976. doi:10.1515/nanoph-2017-0015
66. Morales-Masis M, Martin De Nicolas S, Holovsky J, De Wolf S, Ballif C. Low-temperature high-mobility amorphous IZO for silicon heterojunction solar cells. *IEEE J Photovoltaics*. 2015;5(5):1340-1347. doi:10.1109/JPHOTOV.2015.2450993
67. Ni ZH, Wang HM, Kasim J, et al. Graphene thickness determination using reflection and contrast spectroscopy. *Nano Lett*. 2007;7(9):2758-2763. doi:10.1021/nl071254m
68. Collin S, Raoult E, Bodeux R, Jutteau S, Rives S, Yaiche A, Coutancier D, Rousset J, "Optical characterizations and modelling of semitransparent perovskite solar cells for tandem applications," 36th European Photovoltaic Solar Energy Conference and Exhibition (EU PVSEC), pp. 757–763, 2019, doi:10.4229/EUPVSEC20192019-3BV.2.53.
69. Holman ZC, Filipič M, Descoeudres A, et al. Infrared light management in high-efficiency silicon heterojunction and rear-passivated solar cells. *J Appl Phys*. 2013;113(1):013107. doi:10.1063/1.4772975
70. Barraud L, Holman ZC, Badel N, et al. Hydrogen-doped indium oxide/indium tin oxide bilayers for high-efficiency silicon heterojunction solar cells. *Sol Energy Mater Sol Cells*. 2013;115:151-156. doi:10.1016/J.SOLMAT.2013.03.024
71. Chen JH, Jang C, Xiao S, Ishigami M, Fuhrer MS. Intrinsic and extrinsic performance limits of graphene devices on SiO 2. *Nat Nanotechnol*. 2008;3(4):206-209. doi:10.1038/nnano.2008.58
72. Song Y, Fang W, Hsu AL, Kong J. Iron(III) chloride doping of CVD graphene. *Nanotechnology*. 2014;25(39):395701. doi:10.1088/0957-4484/25/39/395701
73. Novoselov KS, Geim AK, Morozov SV, et al. Electric field in atomically thin carbon films. *Science*. 2004;306(5696):666-669. doi:10.1126/science.1102896
74. Chen JH, Jang C, Adam S, Fuhrer MS, Williams ED, Ishigami M. Charged-impurity scattering in graphene. *Nat Phys*. 2008;4(5):377-381. doi:10.1038/nphys935
75. Gosling JH, Makarovsky O, Wang F, et al. Universal mobility characteristics of graphene originating from charge scattering by ionised

impurities. *Commun Phys*. 2021;4(1):1-8. doi:10.1038/s42005-021-00518-2
76. Paradisi A, Biscaras J, Shukla A. Space charge induced electrostatic doping of two-dimensional materials: graphene as a case study. *Appl Phys Lett*. 2015;107(14):143103. doi:10.1063/1.4932572
77. Bonilla RS, Wilshaw PR. A technique for field effect surface passivation for silicon solar cells. *Appl Phys Lett*. 2014;104(23):232903. doi:10.1063/1.4882161
78. Bonilla RS, Wilshaw PR. Potassium ions in SiO2: electrets for silicon surface passivation. *J Phys D Appl Phys*. 2017;51(2):025101. doi:10.1088/1361-6463/AA9B1B
79. Li X, Cai W, An J, et al. Large-area synthesis of high-quality and uniform graphene films on copper foils. *Science*. 2009;324(5932):1312-1314. doi:10.1126/science.1171245
80. Shahin MM. Mass-spectrometric studies of corona discharges in air at atmospheric pressures. *J Chem Phys*. 1966;45(7):2600-2605. doi:10.1063/1.1727980
81. Shahin MM. Nature of charge carriers in negative coronas. *Appl Optics*. 1969;8(101):106-110. doi:10.1364/AO.8.S1.000106
82. Anand A, Islam MM, Meitzner R, Schubert US, Hoppe H. Introduction of a novel figure of merit for the assessment of transparent conductive electrodes in photovoltaics: exact and approximate form. *Adv Energy Mater*. 2021;11(26):2100875. doi:10.1002/AENM.202100875
83. Bonilla RS, Jennison N, Clayton-Warwick D, Collett KA, Rands L, Wilshaw PR. Corona charge in SiO2: kinetics and surface passivation for high efficiency silicon solar cells. *Energy Procedia*. 2016;92:326-335. doi:10.1016/J.EGYPRO.2016.07.090
84. Pirkle A, Chan J, Venugopal A, et al. The effect of chemical residues on the physical and electrical properties of chemical vapor deposited graphene transferred to SiO2. *Appl Phys Lett*. 2011;99(12):122108. doi:10.1063/1.3643444
85. Yu M, Shi Y, Deru J, et al. Assessing the potential of inversion layer solar cells based on highly charged dielectric nanolayers. *Phys Status Solidi Rapid Res Lett*. 2021;15(12):2100129. doi:10.1002/pssr.202100129
86. Jia Y, Gong X, Peng P, et al. Toward high carrier mobility and low contact resistance: laser cleaning of PMMA residues on graphene surfaces. *Nano-Micro Lett*. 2016;8(4):336-346. doi:10.1007/S40820-016-0093-5/FIGURES/6
87. Dan Y, Lu Y, Kybert NJ, Luo Z, Johnson ATC. Intrinsic response of graphene vapor sensors. *Nano Lett*. 2009;9(4):1472-1475. doi:10.1021/nl8033637
88. Lee H, Paeng K, Kim IS. A review of doping modulation in graphene. *Synth Met*. 2018;244:36-47. doi:10.1016/J.SYNTHMET.2018.07.001
89. Berger C, Song Z, Li X, et al. Electronic confinement and coherence in patterned epitaxial graphene. *Science*. 2006;312(5777):1191-1196. doi:10.1126/science.1125925
90. Leong WS, Wang H, Yeo J, et al. Paraffin-enabled graphene transfer. *Nat Commun*. 2019;10(1):1-8. doi:10.1038/s41467-019-08813-x
91. Ferrari AC, Meyer JC, Scardaci V, et al. *Raman spectrum of graphene and graphene layers*; 2006. doi:10.1103/PhysRevLett.97.187401
92. Fates R, Bouridah H, Raskin J-P. Probing carrier concentration in gated single, bi- and tri-layer CVD graphene using Raman spectroscopy. *Carbon N Y*. 2019;149:390-399. doi:10.1016/j.carbon.2019.04.078
93. Bruna M, Ott AK, Ijäs M, Yoon D, Sassi U, Ferrari AC. Doping dependence of the Raman spectrum of defected graphene. *ACS Nano*. 2014;8(7):7432-7441. doi:10.1021/nn502676g
94. Das A, Pisana S, Chakraborty B, et al. Monitoring dopants by Raman scattering in an electrochemically top-gated graphene transistor. *Nat Nanotechnol*. 2008;3(4):210-215. doi:10.1038/nnano.2008.67
95. Li W, Cheng G, Liang Y, et al. Broadband optical properties of graphene by spectroscopic ellipsometry. *Carbon*. 2016;99:348-353. doi:10.1016/J.CARBON.2015.12.007
96. Ma X, Zhang H. Fabrication of graphene films with high transparent conducting characteristics. *Nanoscale Res Lett*. 2013;8(1):1-6. doi:10.1186/1556-276X-8-440/FIGURES/6
97. Tyagi A, Mišeikis V, Martini L, et al. Ultra-clean high-mobility graphene on technologically relevant substrates. *Nanoscale*. 2022;14(6):2167-2176. doi:10.1039/D1NR05904A
98. "*Monolayer graphene on 8-inch (200mm) diameter Si/SiO2 wafer - GROLLTEX - GRAPHENE-ROLLING-TECHNOLOGIES*." Accessed July 19, 2022. https://grolltex.com/product/contiguous-monolayer-graphene-8-inch-200mm-diameter-si-sio2-wafer/
99. Macco B, Wu Y, Vanhemel D, Kessels WMM. High mobility In_2O_3:H transparent conductive oxides prepared by atomic layer deposition and solid phase crystallization. *Phys Status Solidi Rapid Res Lett*. 2014;8(12):987-990. doi:10.1002/PSSR.201409426
100. Han C, Zhao Y, Mazzarella L, et al. Room-temperature sputtered tungsten-doped indium oxide for improved current in silicon heterojunction solar cells. *Sol Energy Mater Sol Cells*. 2021;227:111082. doi:10.1016/J.SOLMAT.2021.111082
101. Shivayogimath A, Whelan PR, Mackenzie DMA, et al. Do-it-yourself transfer of large-area graphene using an office laminator and water. *Chem Mater*. 2019;31(7):2328-2336. doi:10.1021/acs.chemmater.8b04196
102. Zhao Y, Song Y, Hu Z, et al. Large-area transfer of two-dimensional materials free of cracks, contamination and wrinkles via controllable conformal contact. *Nat Commun*. 2022;13(1):1-10. doi:10.1038/s41467-022-31887-z
103. Usui T, Donnelly CA, Logar M, Sinclair R, Schoonman J, Prinz FB. Approaching the limits of dielectric breakdown for SiO2 films deposited by plasma-enhanced atomic layer deposition. *Acta Mater*. 2013;61(20):7660-7670. doi:10.1016/J.ACTAMAT.2013.09.003
104. Alexandrov SE, McSporran N, Hitchman ML. Remote AP-PECVD of silicon dioxide films from hexamethyldisiloxane (HMDSO). *Chem Vap Depos*. 2005;11(11–12):481-490. doi:10.1002/CVDE.200506385
105. Xin H, Li W. A review on high throughput roll-to-roll manufacturing of chemical vapor deposition graphene. *Appl Phys Rev*. 2018;5(3):031105. doi:10.1063/1.5035295/14573816/031105_1_ACCEPTED_MANUSCRIPT.PDF
106. Polsen ES, McNerny DQ, Viswanath B, Pattinson SW, John Hart A. High-speed roll-to-roll manufacturing of graphene using a concentric tube CVD reactor. *Sci Reports*. 2015;5(1):1-12. doi:10.1038/srep10257
107. Hu Z, Li F, Wu H, et al. Rapid and scalable transfer of large-area graphene wafers. *Adv Mater*. 2023;35(29):2300621. doi:10.1002/ADMA.202300621

SUPPORTING INFORMATION

Additional supporting information can be found online in the Supporting Information section at the end of this article.

How to cite this article: O'Sullivan J, Wright M, Niu X, Miller P, Wilshaw PR, Bonilla RS. Towards a graphene transparent conducting electrode for perovskite/silicon tandem solar cells. *Prog Photovolt Res Appl*. 2023;1-15. doi:10.1002/pip.3739